High-Speed, Ultrahigh-Resolution Spectral-Domain OCT with Extended Imaging Range Using Reference Arm Length Matching

tvst

Article

High-Speed, Ultrahigh-Resolution Spectral-Domain OCT with Extended Imaging Range Using Reference Arm Length Matching

ByungKun Lee[1,†], Siyu Chen[1,†], Eric M. Moult[1], Yue Yu[1], A. Yasin Alibhai[2], Nihaal Mehta[2], Caroline R. Baumal[2], Nadia K. Waheed[2], and James G. Fujimoto[1]

[1] Department of Electrical Engineering and Computer Science, Research Laboratory of Electronics, Massachusetts Institute of Technology, Cambridge, MA, USA
[2] New England Eye Center, Tufts University School of Medicine, Boston, MA, USA

Correspondence: James G. Fujimoto, Department of Electrical Engineering and Computer Science, Research Laboratory of Electronics, Massachusetts Institute of Technology, Cambridge, MA, USA. e-mail: jgfuji@mit.edu

Received: September 9, 2019
Accepted: April 2, 2020
Published: June 8, 2020

Keywords: Optical coherence tomography; ultrahigh-resolution OCT; spectral domain OCT; age-related macular degeneration

Citation: Lee B, Chen S, Moult EM, Yu Y, Alibhai AY, Mehta N, Baumal CR, Waheed NK, Fujimoto JG. High-speed, ultrahigh-resolution spectral-domain OCT with extended imaging range using reference arm length matching. Trans Vis Sci Tech. 2020;9(7):12, https://doi.org/10.1167/tvst.9.7.12

Purpose: To develop high-speed, extended-range, ultrahigh-resolution spectral-domain optical coherence tomography (UHR SD-OCT) and demonstrate scan protocols for clinical retinal imaging.

Methods: A UHR SD-OCT operating at 840-nm with 150-nm bandwidths was developed. The axial imaging range was extended by dynamically matching reference arm length to the retinal contour during acquisition. Two scan protocols were demonstrated for imaging healthy participants and patients with dry age-related macular degeneration. A high-definition raster protocol with intra–B-scan reference arm length matching (ReALM) was used for high-quality cross-sectional imaging. A cube volume scan using horizontal and vertical rasters with inter–B-scan ReALM and software motion correction was used for en face and cross-sectional imaging. Linear OCT signal display enhanced visualization of outer retinal features.

Results: UHR SD-OCT was demonstrated at 128- and 250-kHz A-scan rates with 2.7 µm axial resolution and a 1.2-mm, 6-dB imaging range in the eye. Dynamic ReALM was used to maintain the retina within the 6-dB imaging range over wider fields of view. Outer retinal features, including the rod and cone interdigitation zones, retinal pigment epithelium, and Bruch's membrane were visualized and alterations observed in age-related macular degeneration eyes.

Conclusions: Technological advances and dynamic ReALM improve the imaging performance and clinical usability of UHR SD-OCT.

Translational Relevance: These advances should simplify clinical imaging workflow, reduce imaging session times, and improve yield of high quality images. Improved visualization of photoreceptors, retinal pigment epithelium, and Bruch's membrane may facilitate diagnosis and monitoring of age-related macular degeneration and other retinal diseases.

Introduction

Optical coherence tomography (OCT)[1] imaging of the human retina[2,3] has substantially improved the diagnosis, monitoring, and treatment of retinal and optic nerve diseases. OCT can resolve fine layered features because the axial resolution is decoupled from the optical depth of focus, which is limited by the anatomy of the eye and optical aberrations. Ultrahigh-resolution (UHR) OCT uses broadband light sources to achieve axial resolutions below the 5-to 7-µm range of standard commercial OCT instruments.[4–7] Multiplexed superluminescent diodes with 840-nm center wavelength are often used in UHR spectral/Fourier-domain OCT (SD-OCT) and early studies demonstrated improved visualization of photoreceptor impairment, retinal pigment epithelium

(RPE) disruption, drusen, and pigment migration, which are important markers of age-related macular degeneration (AMD) progression.[8–14] The finest axial resolution reported to date was achieved using visible-light illumination OCT, where submicrometer performance was demonstrated in vivo.[15–17] However, clinical adoption of using visible-light illumination OCT is likely to be limited in the near future due to the high cost and limited availability of low-noise visible-light sources, lower laser exposure limits, and patient discomfort.

The limited imaging range of UHR SD-OCT at 840 nm has been a substantial barrier to its clinical adoption. To achieve fine axial resolution, the OCT spectrometer should be designed to cover a broad wavelength range by compromising the spectral resolution—the wavelength difference between adjacent line-scan camera pixels. UHR SD-OCT has a limited axial image range because imaging range is inversely related to spectral resolution. Further complicating this issue, UHR OCT imaging requires finer transverse spatial sampling of the retina, mandating higher acquisition speeds. This choice leads to a critical trade-off between the imaging range and speed. For example, an earlier prototype high-speed SD-OCT instrument used only 576 pixels out of a 4096-pixel line-scan camera (Basler Sprint) to achieve 312.5 kHz A-scan rate.[18] This strategy decreased the imaging range to ~0.8 mm in air (~0.6 mm in tissue). Complex SD-OCT designs have addressed this trade-off by using multiple line-scan cameras[19] or area-scan cameras[20]; however, sufficient depth range for reliable clinical application has not yet been achieved. Swept-source/Fourier-domain OCT enables fast A-scan rates and fine spectral resolution to achieve long range. However, retinal swept-source/Fourier-domain OCT is currently only available at 1050 nm, where UHR retinal imaging is not feasible because the spectral bandwidth is limited by the narrow transmission window of the vitreous.[21]

The axial imaging range is especially important for wide field of view (FOV) volumetric imaging, because the retina is curved and becomes displaced in the axial direction during OCT beam scanning. This axial displacement is appreciable in larger FOV acquisitions and in patients with high myopia or tilted discs. Although this effect can be mitigated by montaging several smaller FOV acquisitions, montaging requires multiple OCT acquisitions with different fixation positions, increasing the imaging time and procedural complexity. Moreover, eyes with ocular opacities sometimes require moving the instrument away from the pupil center, tilting the retinal image. Patient head motion can also produce variations in the axial eye position. These effects complicate both alignment and image acquisition, leading to prolonged imaging sessions and higher rates of poor image quality. For example, if the retina overlaps the reference arm zero-delay position, "zero-delay crossing" or "mirror" artifacts appear. Conversely, if the retina moves too far from the zero-delay position, signal roll-off effect occurs.

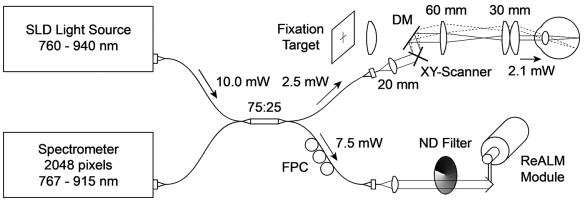

Figure 1. Schematic diagram of the UHR SD-OCT system. The longer wavelength edge of the light source spectrum was cut off to optimize the trade off between higher axial resolution and longer imaging range. DM, dichroic mirror; FPC, fiber polarization controller; ND, neutral density; SLD, superluminescent diode.

In this article, we present a series of technical developments that address the aforementioned limitations and thereby promise to facilitate widespread clinical adoption. New camera technology and revised laser safety standards[22] enable faster imaging. Improved spectrometer design reduces depth-dependent sensitivity roll-off and alleviates the trade-off between the axial resolution and range. Reference arm length matching (ReALM) dynamically tracks the retinal contour, extending the effective imaging range for large FOV scans. Finally, selective linear display of the OCT signal amplitude preserves the image resolution for fine structures in the outer retina. Representative imaging examples from healthy participants and patients with nonexudative AMD are presented. Special emphasis is placed on the ability to visualize alterations in the photoreceptors, RPE, and Bruch's membrane (BM), which are potential markers of AMD progression.

Methods

UHR SD-OCT Instrument Design

Figure 1 shows a schematic of the SD-OCT system. A commercially available, multiplexed superluminescent diode light source (cBLMD-T-850-HP-I, Superlum, Cork, Ireland) spanning 760 nm to 940 nm wavelength with ~10 mW output power (Fig. 2A) was used as the broadband light source. A broadband fiberoptic 75:25 splitter distributed the power to the reference and the sample arms, respectively. The patient imaging interface had a collimator

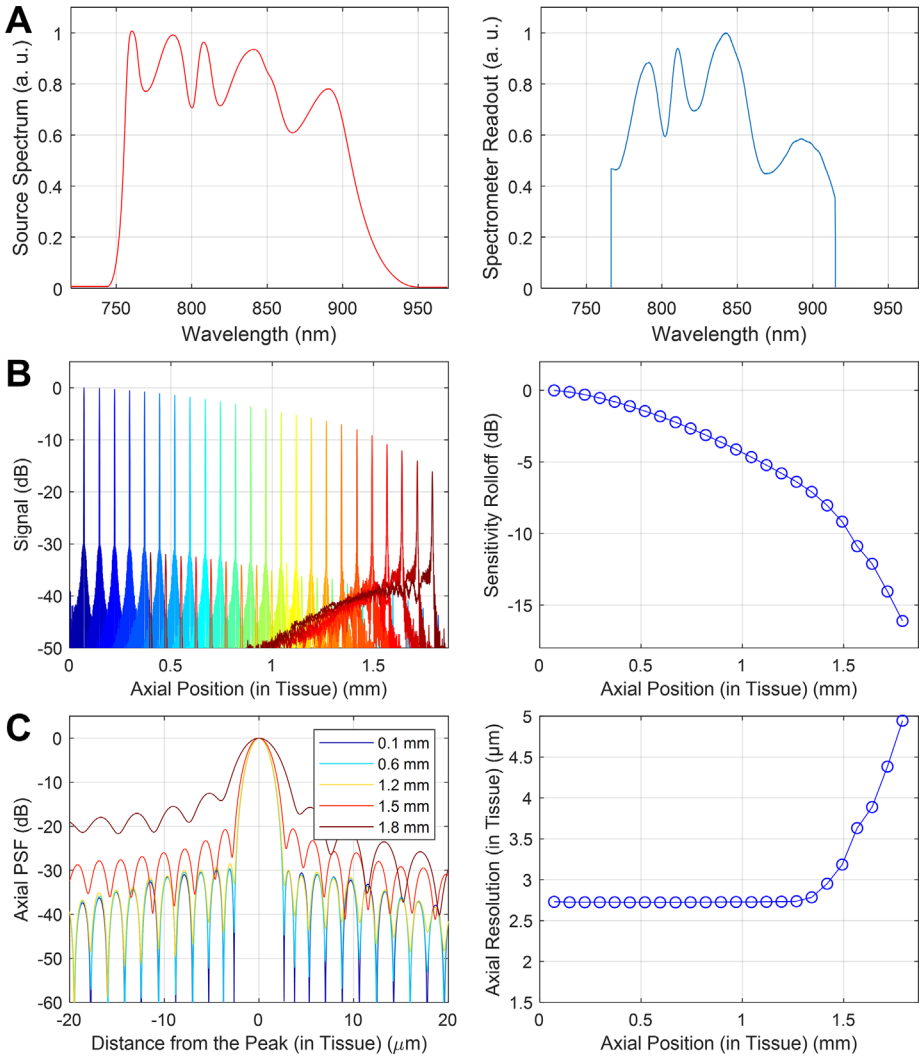

Figure 2. (A) Source power spectrum measured by an optical spectrum analyzer at the laser output and the reference arm spectrum received by the OCT spectrometer. (B) Signal roll-off represented by the point spread functions and their peak magnitudes plotted as a function of axial position. (C) Axial point spread function at various axial positions and the full width at half-maximum (FWHM) axial resolution plotted as a function of axial position.

(f = 20 mm), galvanometer mirror scanners (5 mm clear aperture, 6215H, Cambridge Technology, Cambridge, MA), scan lens (f = 60 mm, ø = 30 mm), and ocular lens (f = 30 mm, ø = 30 mm). The incident beam was 2.4 mm wide (diameter at $1/e^2$ intensity) on the cornea with 2.1 mW power, within the revised safety limit according to the American National Standards Institute.[22] Because many previous 840-nm SD-OCT instruments used a 0.75 mW exposure under earlier American National Standards Institute standards,[23] this increase in exposure enables a proportionate increase in imaging speed while maintaining sensitivity. A laser interlock using an independent microcontroller monitored the galvanometer scanners and laser power, blocking the beam if the scanners stopped or laser power increased.

The spectrometer was built by a commercial manufacturer (Cobra-S C-00359, Wasatch Photonics, Durham, NC) to our design specifications for wavelength range of 767 nm to 915 nm. We chose this wavelength range to optimize image axial resolution by avoiding high absorption in the vitreous at longer wavelengths, while preserving sufficient spectral resolution to maintain imaging range. The interference spectrum was detected using a new high speed, 2048-pixel line-scan CMOS camera (OctoPlus, e2v, Chelmsford, UK) which can support line rates from 80 kHz to 250 kHz. The camera output was recorded by a Camera Link frame grabber (Xcelera-CL+ PX8 Full, Teledyne DALSA, Billerica, MA) with a maximum data width of 80 bits, which can capture the full 12 bits of the camera pixels at line rates of up to 128 kHz, and

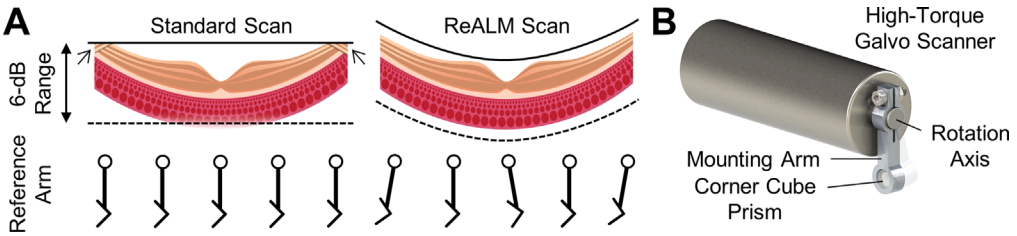

Figure 3. (A) Visual explanation of ReALM. Retinal SD-OCT scans of moderate to wide fields of view (FOV) may be susceptible to "zero-delay crossing" artifacts, indicated by the arrows near the top of the B-scan and sensitivity roll-off at deeper parts of the image. Dynamically adjusting the reference arm optical path length during OCT scan moves the axial imaging window to maintain the retina within the high signal range close to, but strictly below, the top of the imaging range. (B) A three-dimensional model of the ReALM module showing how the reference arm optical path length can be rapidly adjusted to move the axial imaging window.

10 bits up to 250 kHz. All 2048 pixels on the camera were used for OCT interference signal detection.

Figure 2 shows the axial imaging performance. The axial resolution was 2.4 µm full-width at half-maximum (FWHM) in tissue ($n = 1.3375$) using the spectrum directly from the light source and 2.7 µm full-width at half-maximum with a Taylor-windowed spectrum for reduced side lobes. The 6-dB sensitivity roll-off imaging range was 1.2 mm in tissue, as shown in Figure 2B. This improvement is notable over earlier UHR SD-OCT instruments, which had substantially less than a 1-mm imaging range.[18] Using appropriate image processing described later in this paper, the axial resolution was nearly constant up to 1.4 mm in tissue, as shown in Figure 2C. This feature is important for quantitative measurements. The detection sensitivity defined by the signal-to-noise ratio limit near the zero delay was 102.4 dB at 128 kHz A-scan rate and 99.1 dB at 250 kHz A-scan rate.

ReALM and Scan Protocols

Although the 1.2-mm, 6-dB imaging range in tissue is an improvement from previous UHR SD-OCT instruments, it is still insufficient for clinical imaging studies. Therefore, we extended the effective imaging range using dynamic ReALM, which rapidly adjusts the reference arm optical path length to track the retinal contour during acquisition (Fig. 3). This technique enables extended FOV even with a limited imaging range. The ReALM module consisted of a small corner cube prism mounted on a high-torque galvanometer scanner (6240H, Cambridge Technologies, MA) as shown in Figure 3B. The reference arm length can be programmed to follow the retinal contour as illustrated in Figure 4A. The implementation of ReALM is analogous to axial scanning in early time-domain OCT and phase shifters used in some full-range OCT instruments.[24,25] Modulating the reference arm using a galvanometer scanner introduces a small angular displacement of the corner cube prism. However, due to the low reference arm coupling ratio and the short modulation length, the subsequent fluctuation in the OCT fringe is inconsequential. This effect can be further reduced using the signal processing procedures outlined in the Supplementary Materials.

For longer B-scans with a high number of A-lines, the reference arm length can track retinal contour in the fast-scan direction (intra–B-scan ReALM) without noticeable signal loss from fringe washout effects.[26] However, for fast B-scans with lower A-scan densities, tracking retinal contour along the fast scan direction will reduce the OCT signal and the retinal contour can only be tracked between sequential B-scans, in the slow scan direction (inter–B-scan ReALM). Finally, fringe washout can also occur from rapid transverse scanning itself, even if the reference arm length is not varied. Because signal loss from fringe washout depends on multiple factors, such as the ReALM tracking speed, transverse scan speed, camera integration time per A-scan, and patient imaging optics, scan protocol parameters must be carefully determined based on the image quality. A guideline for maximum ReALM tracking speeds to avoid excessive fringe washout is presented in the discussion. Figure 4 shows a representative high-definition (HD) B-scan comprising 12,000 A-scans along a 12-mm horizontal cross-section through the fovea acquired in 0.1 seconds with intra–B-scan ReALM. Fine layered features in the outer retina can be clearly resolved (Fig. 4B–D).

Using the higher acquisition speeds enabled by new line scan camera technology and increased retinal exposure safety standards, we developed two scan protocols: an HD raster and a cube volume. The HD raster scan was optimized for visualizing fine cross-sectional features in the outer retina, while the cube volume scan was optimized for comprehensive three-dimensional imaging and en face analysis. The HD raster consisted of 241 B-scans, each containing 1800 A-scans, over a 9 mm × 6 mm

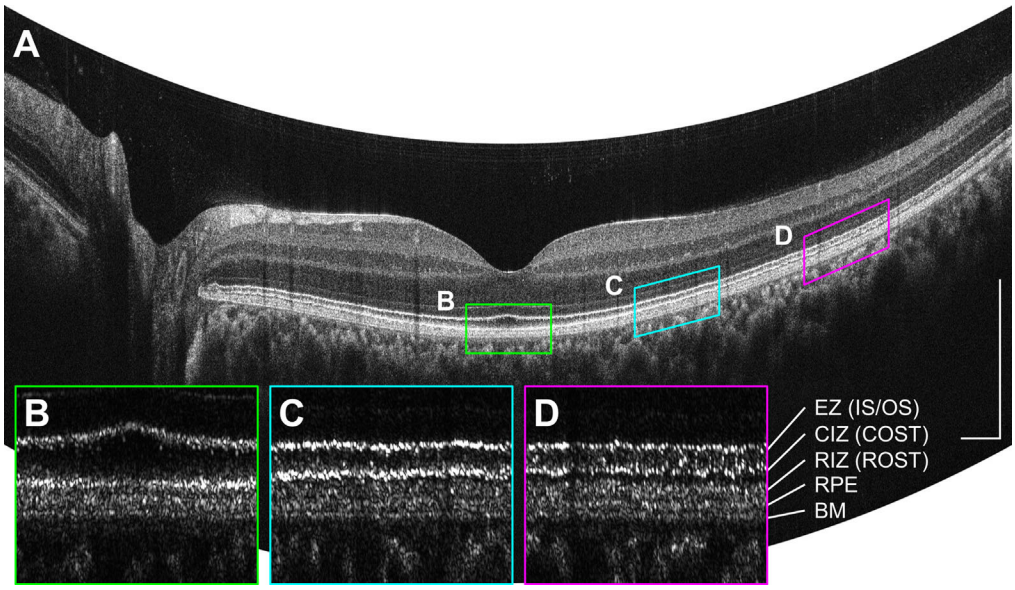

Figure 4. (A) A 12-mm horizontal high-definition (HD) scan comprising 12,000 A-scans, acquired with intra–B-scan ReALM. (B–D) BM-flattened enlargements of the 1 mm × 200 µm areas demarcated by the colored lines, plotted in linear OCT signal display. The CIZ (COST) seemed to be brightest near the fovea (B), while the RIZ (ROST) seemed to be brightest at 4 mm temporal to the fovea (D) consistent with cone–rod distribution. CIZ, cone interdigitation zone; COST, cone outer segment tips; EZ, ellipsoid zone; IS/OS, inner segment/outer segment junction; RIZ, rod interdigitation zone; ROST, rod outer segment tips. Scale bars: 500 µm.

FOV. The cube volume was generated by software-motion correcting and merging two perpendicular raster scan volumes (i.e., horizontal-fast and vertical-fast),[27–29] each of which comprised 500 × 500 A-scans (or 750 x 750 A-scans) over a 9 mm × 9 mm FOV or a 6 mm × 6 mm FOV.

By dynamically adjusting the reference arm length, ReALM axially shifts the retinal image position so it seems to be less curved. We used two remapping approaches to recover the true retinal contour: reference arm length trajectory inversion and software motion correction. Trajectory inversion corrects the axial positions of inter–B-scan and intra–B-scan ReALM images by shifting the A-scans to compensate the trajectory used to drive the ReALM module. Software motion correction is applied to cube volume only, and uses perpendicular raster scans to estimate the true retina contour in all three dimensions.[27–29] Throughout this paper, all images have been corrected to display true retinal contour unless otherwise noted.

Computing the ReALM Trajectory

To estimate the ReALM trajectory, the retinal contour was modeled as a two-dimensional surface $z = f(x, y)$. The axial coordinate z was modeled into a quadratic polynomial function of the transverse coordinates x (horizontal) and y (vertical):

$$z = f(x, y) = c(x^2 + y^2) + t_x x + t_y y. \quad (1)$$

The second-order coefficient c represents the curvature, while the first-order coefficients t_x and t_y represent the tilt. These coefficients were estimated in real-time using a central horizontal (horizontal-fast) B-scan and a central vertical (vertical-fast) B-scan. The estimation process involved four steps: (i) the pilot B-scans were filtered with a Gaussian kernel to reduce noise; (ii) high-intensity pixels were selected using a constant, empirically determined threshold; (iii) for each A-scan, an axial position—$z_x(x)$ for the horizontal-fast B-scan, and $z_y(y)$ for the vertical-fast B-scan—was computed as the "center of mass" of the selected pixels along that A-scan, where the "mass" of a pixel was equal to its OCT signal; and (iv) the $z_x(x)$ and $z_y(y)$ signals are fitted with quadratic univariate polynomials,

$$\begin{aligned} \hat{z}_x &= \hat{c}_x x^2 + \hat{t}_x x + \hat{z}_{0x}, \\ \hat{z}_y &= \hat{c}_y y^2 + \hat{t}_y y + \hat{z}_{0y}, \end{aligned} \quad (2)$$

respectively. The value of c in (1) was taken as the average of the second order coefficient estimates, $\hat{c}_x$ and $\hat{c}_y$, of the fitted polynomials, while the values of t_x and t_y were taken as the first order coefficients from the fitted polynomials, $\hat{t}_x$ and $\hat{t}_y$, respectively. The constant terms corresponded to the axial position of the center

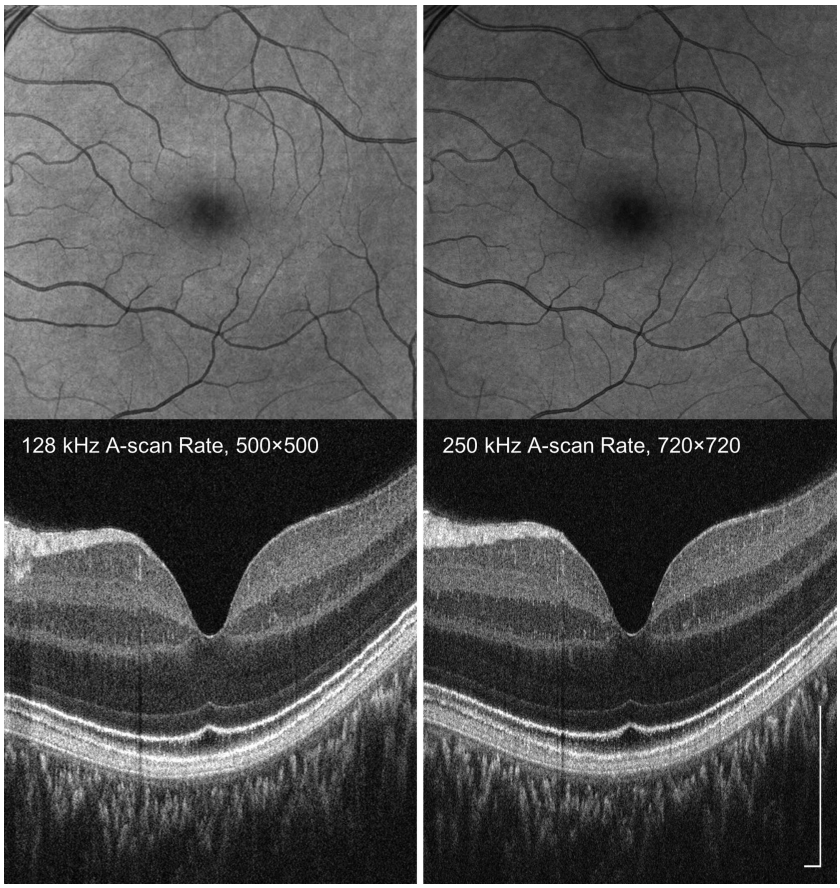

Figure 5. Comparison of motion-corrected volumes acquired at 128 kHz and 250 kHz A-scan rates. A 6 mm × 6 mm macular volume of a healthy eye was acquired using 500 × 500 raster scans at 128 kHz A-scan rate and 720 × 720 raster scans at 250 kHz A-scan rate, respectively. Acquisition times per scan were 2.3 seconds at 128 kHz and 2.4 seconds at 250 kHz. Slower A-scan rates have high signal to noise, whereas high A-scan rates enable denser transverse sampling improving en face image resolution. Scale bars: 250 µm.

of the scan and were not used for ReALM trajectory calculation.

Participant Recruitment

Images of healthy control eyes and eyes with nonexudative AMD were acquired at the New England Eye Center at Tufts Medical Center (Boston, MA) under protocols approved by the Tufts Medical Center IRB and the Massachusetts Institute of Technology Committee for the Use of Humans as Experimental participants. Written informed consent was obtained from the patients before imaging and procedures were compliant with the declaration of Helsinki.

Results

We evaluated the instrument by imaging six normal eyes from six healthy participants (age 41.8 ± 22.2 years) and nine eyes with nonexudative AMD from eight patients (age 78.0 ± 9.9 years), one of whom had geographic atrophy (GA). Typical levels of ocular opacity were observed in eyes with nonexudative AMD.

Comparison Between 128 kHz and 250 kHz A-Scan Rates

Figure 5 shows a representative comparison of imaging performance at 128 kHz and 250 kHz A-scan rates in a healthy participant with no ocular opacity. Cube volumes covering 6 mm × 6 mm area were acquired at 128 kHz and 250 kHz A-scan rates. Each raster scan acquisition comprised 500 × 500 A-scans for 128 kHz and 720 × 720 for 250 kHz A-scan rates, with acquisition times of 2.3 and 2.4 seconds, respectively. The B-scans showed that signal level was higher for the 128 kHz A-scan rate as expected; meanwhile, en face images showed that higher sampling density at

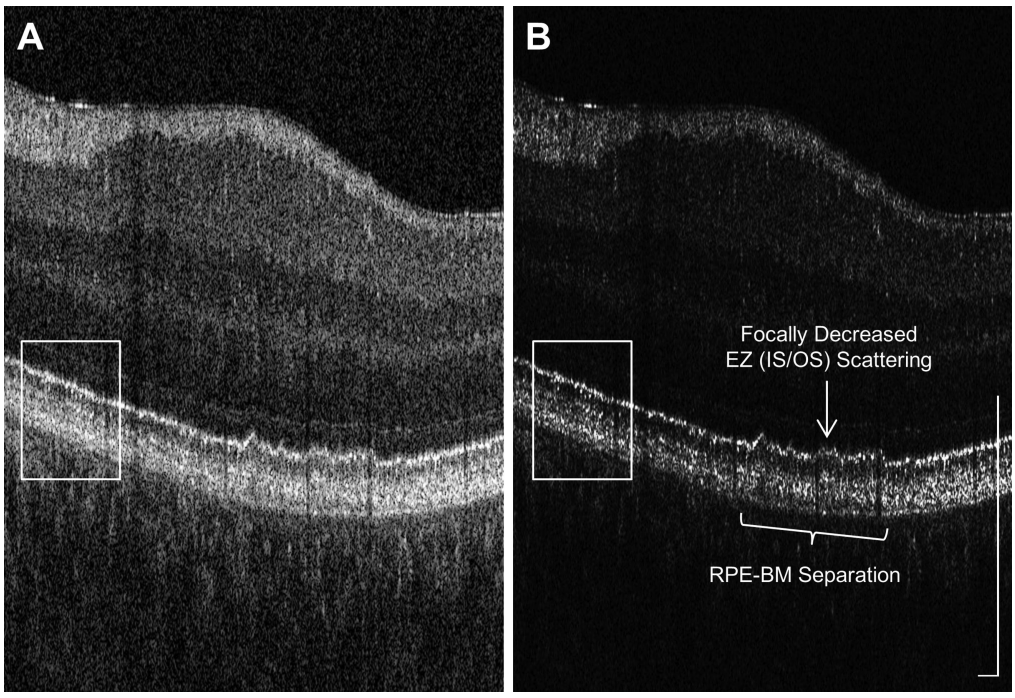

Figure 6. Comparison of display scales for viewing UHR OCT images. The same B-scan, extracted from a 6 mm × 6 mm, *x*-fast, 500 × 500 A-scan volume taken from an eye with early nonexudative AMD, was plotted in (A) logarithmic display and (B) linear display. AMD-related features such as the RPE–BM separation and focally decreased ellipsoid zone (inner segment/outer segment junction) scattering can be more clearly visualized in linear display because it preserves axial and transverse resolution compared with a logarithmic display. Scale bars: 250 µm.

250 kHz A-scan rate enhances visualization of structures such as small retinal blood vessels. Furthermore, the higher sampling density may also enhance the transverse accuracy of software motion correction, because the algorithm performs subpixel shifts of the A-scans. Higher sampling density can also be achieved at slower imaging speeds by extending the image acquisition times to several seconds using eye tracking.

Greater sensitivity is important for imaging eyes with ocular opacities or astigmatism, and therefore the lower 128 kHz A-scan rate was chosen for imaging patients. The higher 250 kHz A-scan rate may be useful in selected eyes without cataracts, vitreal alterations, or appreciable astigmatism because high speed allows denser scanning, wider FOV, and improved performance for modalities such as OCT angiography and Doppler OCT. Higher speeds may also become feasible for patient imaging if camera sensitivities improve in the future.

Image Display for Visualizing Outer Retinal Features

OCT B-scans are typically displayed using the logarithm of the OCT signal amplitude because the backscattering signal can vary by orders of magnitude in different retinal layers. Logarithmic display enhances dynamic range, enabling weakly scattering structures such as the nuclear layers and highly scattering structures such as the RPE to be visualized in the same image. However, logarithmic display causes sharp signal peaks to appear substantially broader, resulting in a loss of axial and transverse resolution. Linear display of the OCT signal amplitude, which is proportional to the backscattered electric field amplitude or the square root of intensity, improves the visualization of fine, bright features. This property explains why linear OCT signal display has been used for displaying high-resolution adaptive optics OCT images.[30–33] Therefore, we have used linear OCT signal display when showing BM-flattened outer retinal slabs, such as in Figure 4B to 4D. Figure 6 shows another example where linear display can be more useful than logarithmic display for visualizing outer retinal changes in AMD eyes. The area inside the box suggests fine layered structure in the outer retina can be resolved clearer in linear display. Moreover, AMD-related features such as the RPE–BM separation and focally decreased scattering in the ellipsoid zone, alternatively referred to as inner segment/outer segment junction, can be more clearly visualized in linear display.

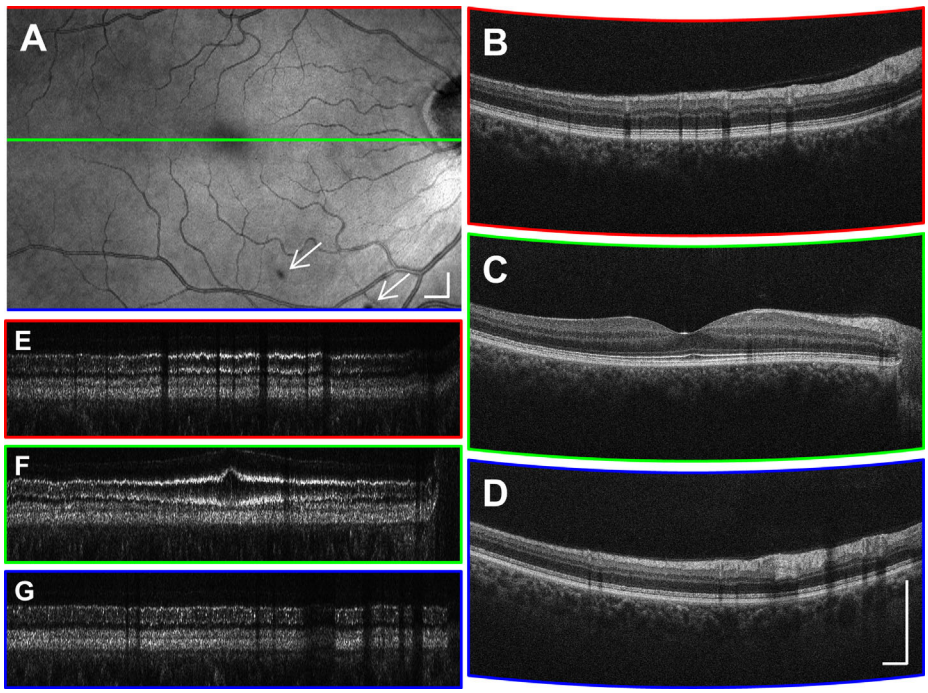

Figure 7. Representative HD raster scan from a 58-year-old healthy participant. (A) The en face projection suggests that the B-scan spacing was adequate for detecting focal shadows (*arrows*). (B–D) A small amount of intra–B-scan ReALM was applied to flatten the retinal contour without producing excessive signal loss from fringe washout effects. (E–G) The BM-flattened 200-um slabs shown in linear display. Scale bars: 500 µm.

High-Definition Raster Scans

The HD raster scan protocol (Fig. 7) was designed for visualizing cross-sectional features, especially the fine layered structures in the outer retina. Figure 7E to 7G shows 200-µm-thick outer retinal slab flattened with reference to the BM, in a linear OCT signal display, where the axial dimension has been enlarged to improve visualization. The B-scans, each containing 1800 A-scans, were chosen from 241 B-scans covering a 9 mm × 6 mm area. Images were acquired in 3.7 seconds at a 128 kHz A-scan rate. Within each B-scan, A-scans are separated by only 5 µm, which improves the effective signal-to-noise ratio and continuity of outer retinal features. Adjacent B-scans are vertically separated by 25 µm, sufficiently close for detecting focal lesions such as focal hyperpigmentation and hard drusen. However, the 25 µm B-scan spacing was insufficient for high-quality en face visualization. In this representative image from an older healthy participant, the outer retinal layers were less sharp compared to that in younger participants (Fig. 4); however, the distinctive ellipsoid zone (inner segment/outer segment junction), cone and rod interdigitation zones (outer segment tips), and RPE/BM layers could still be clearly differentiated.

Motion-Corrected Cube Volumes

Increased imaging speed enables the acquisition of raster-scanned volumes with greater numbers of A-scans, facilitating both cross-sectional and en face visualization. Software motion correction reduces artifacts from eye motion, improving longitudinal analysis of lesion size and en face morphology. Because preserving axial resolution is critical for UHR OCT studies, the axial precision of software motion correction was assessed by comparing the sharpness of the outer retinal features between individual volumes before and after motion correction and merging. Two independent readers inspected volumes from six healthy eyes, and assessed the outer retinal sharpness to be unaffected by software motion correction and merging. In addition to correcting eye motion and recovering true retinal contour, Figure 8 also shows that, in some regions, the signal-to-noise ratio improvement from merging the two cube volumes enhanced outer retinal layer continuity and sharpness by reducing speckle noise in the images.

Figure 9 further demonstrates that inter-B-scan ReALM is compatible with software motion correction, because small displacements of the reference arm length are equivalent to axial eye

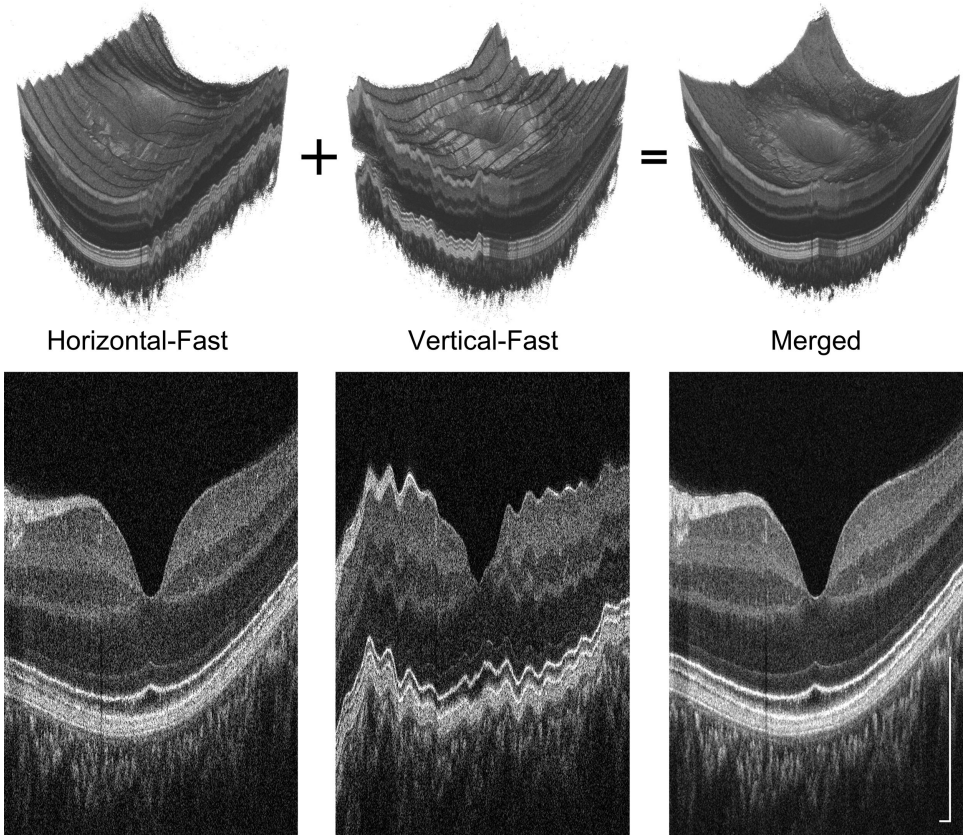

Figure 8. Comparison of the cross-sections from 6 mm × 6 mm volumes before and after software motion correction and merging. The correction was sufficiently precise to maintain the sharpness of the photoreceptor interdigitation zones/outer segment tips, RPE, and BM. Scale bars: 250 µm.

movement. Figure 9A5 to 9A7 and 9B2 to 9B4 show that the image extracted from the acquired volumes in the slow-scan direction appears nearly flat because the reference path length tracks the retinal contour. Figure 9C2 to 9C7 shows that software motion correction restores the retinal contour in the motion-corrected averaged volume.

Imaging AMD Eyes Using Motion-Corrected Cube Volumes

The signal strength and axial resolution were also evaluated in eyes with nonexudative AMD, where OCT signals can be substantially lower than in healthy eyes. Figure 10 shows representative horizontal and vertical B-scans as well as the en face projections of 6 mm × 6 mm cube volumes taken from two eyes with nonexudative AMD, one with drusen and the other with GA. Note that the rod interdigitation zone (rod outer segment tips), RPE, and BM in Figure 10A2 and 10A3 and areas outside of the GA lesion in Figure 10B2 and 10B3 are not as clearly resolved as in the normal retina in Figure 7. These examples are a surrogate for imaging performance of UHR SD-OCT with ReALM in eyes with other retinal diseases. Glaucoma patients and patients with diabetic retinopathy after cataract surgery typically have lower mean age and thus present less ocular opacity than patients with AMD.

Discussion

UHR SD-OCT is particularly suited for assessing changes in the photoreceptors, RPE, and BM,[34–37] which are potential markers of AMD progression. Therefore, optimizing imaging performance in eyes with AMD is critical for demonstrating the utility of UHR SD-OCT. OCT imaging is generally more challenging in AMD than in other retinal pathologies because of higher mean patients age—seating and aligning procedures take extra care; the signal level can

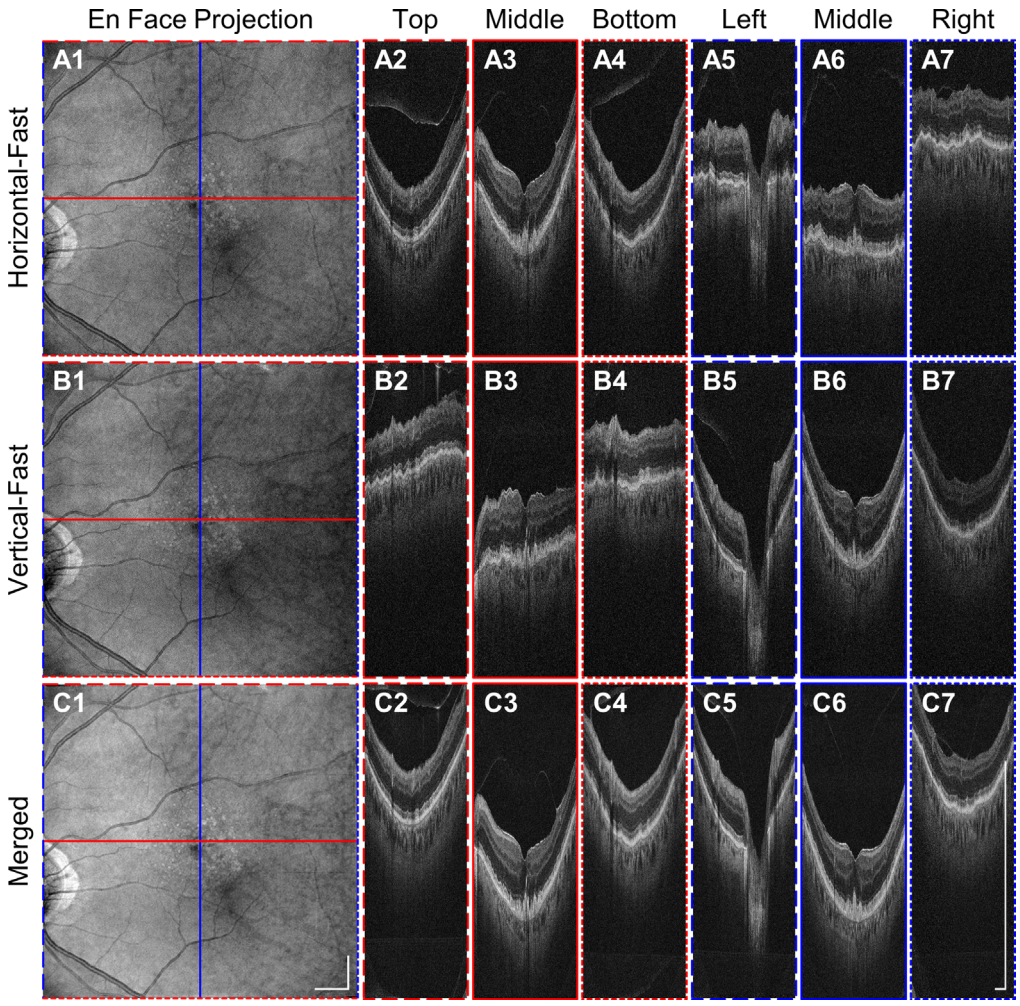

Figure 9. Demonstration of UHR SD-OCT with inter–B-scan ReALM using the software motion corrected volume over a 9 mm × 9 mm macular area in an eye with nonexudative AMD by coregistering two raster scans, each comprising 500 × 500 A-scans. (A1–A7, B1–B7) ReALM automatically compensates for the retinal contour across different B-scans. (C1–C7) software motion correction removes the axial displacement introduced either by patient motion or by ReALM. The result is a motion-free merged volume with enhanced signal. Scale bars: 1 mm.

be severely affected by ocular opacity and/or refractive error. Therefore, we focused on evaluating UHR SD-OCT imaging performance of the HD raster scan and cube volume protocols in AMD.

The HD raster scan uses intra–B-scan ReALM to increase retinal FOV in the fast-scan (horizontal) direction. High pixel density B-scans can reveal alterations in the photoreceptors, RPE, and BM. Selective linear OCT signal display enables visualization of fine features such as the RPE, BM, cone interdigitation zone (cone outer segment tips) and rod interdigitation zone (rod outer segment tips). Cube volumes acquired with inter–B-scan ReALM use software motion correction to achieve comprehensive visualization and en face mapping of focal pathologies, such as drusen and GA. Linear OCT signal display of selected horizontal and vertical B-scans can be used to assess focal alterations in the outer retina.

These functionalities and scan protocols are applicable to commercial SD-OCT and can be achieved with minimal additional cost. Our prototype instrument used a high-torque galvanometer scanner for ReALM; however, voice coils or linear motor stages can also be used at substantially lower cost. Commercial instruments already use active adjustment of reference path length, so the functions of path length adjustment during alignment and dynamic tracking during acquisition can be combined to achieve cost savings. Conversely, in a research prototype instrument, costs are dominated by other components such as the

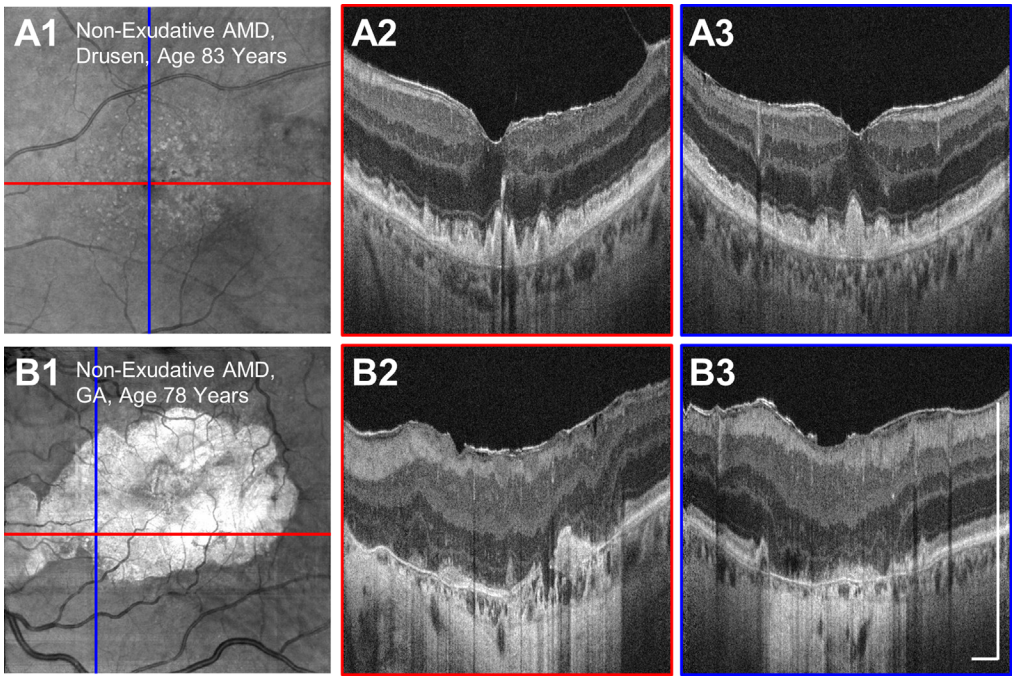

Figure 10. Examples of motion-corrected volumes comprising 500 × 500 A-scans covering 6 mm × 6 mm macular area in nonexudative AMD eyes with drusen (A) and GA (B). Vertical and horizontal B-scans are labeled with red and blue lines, respectively showing that inter–B-scan ReALM maintains the corners of the FOV within the axial imaging range. Scale bars: 500 µm.

spectrometer optics, the line-scan camera, the broadband light source, and the beam-scanning galvanometers, so the fractional additional cost of ReALM is small.

The limitation in the ReALM-modulating speed and the extent to which it can correct retinal contour warrants more discussion. Rapid changes in the reference arm length during the camera integration time causes fringe washout, decreasing the detected OCT signal amplitude. A previous OCT study[38] demonstrate that the sensitivity is penalized by a factor of $(\sin k_0\Delta z/k_0\Delta z)^2$, where k_0 is the center wavenumber and Δz is the total optical path length change during the camera integration time. The axial velocity threshold for severe fringe washout corresponds to the first zero of the sinc function, $v_{\text{washout}} = \lambda_0/4\pi\tau$, where λ_0 is the center wavelength and τ is the camera integration time.[26] This velocity is 27 mm/s at 128 kHz A-line rate. It is important to note that, during retinal imaging, a modulation speed slightly exceeding this limit is still feasible, if the OCT signal is strong enough and remains above the noise background. For scan protocols with rapid B-scans such as the cube volume, we used ReALM only in the slow-scan direction (inter–B-scan ReALM). This strategy reduces variations in axial position of the retina that occur at the corners of the cube volume scan. For scan protocols with slower transverse B-scan rates, such as the HD raster scan, intra–B-scan ReALM also can be performed up to a certain speed limit, extending the effective imaging range and FOV within individual B-scans. However, even for HD raster scans, an intra–B-scan ReALM trajectory with excessive tracking speed can cause fringe washout, especially near the edges where the retinal contour is steeper. Therefore, the ReALM trajectory must be carefully chosen to limit fringe washout effects in intra–B-scan ReALM; retinal contour might be partially compensated by ReALM to trade off sensitivity roll-off versus fringe washout effects.

ReALM can also be compared with other range-extending techniques. Full-range OCT[24,25,39,40] introduces calibrated phase during acquisition to resolve OCT complex conjugate artifacts, effectively doubling the axial imaging range. This phase shift can also be achieved using ReALM, making our instrument compatible with full-range operation. Full-range OCT has the advantage of requiring a lower mirror translating speed, thus avoiding the fringe washout mentioned elsewhere in this article. However, full-range OCT has major limitations. One key limitation is that transverse oversampling is required, making full-range OCT incompatible with rapid cube volume acquisitions. Full-range OCT is also sensitive to eye motion, and small displacements which correspond to a fraction of the wavelength, can cause errors in the complex

conjugate reconstruction, making zero delay image artifacts visible. Finally, full-range OCT cannot extend the image range by more than two times.

Another method sometimes used in clinical practice is changing the working distance between the imaging objective lens and the cornea. By moving the scanning pivot location further into the eye, the apparent retinal contour variation is reduced in OCT images. This approach does not involve dynamic adjustment of the reference arm length and therefore does not suffer from fringe washout. However, it has two critical limitations compared with ReALM. First, there is an increased likelihood of beam vignetting during acquisition because the scanning pivot is moved away from the pupil plane. Second, the transverse scale is changed because the length per unit scan angle decreases as the scanning pivot moves closer to the retina. Therefore, properly setting the working distance so that scanning pivot is at the participant's pupil plane is important for all OCT imaging, regardless of whether ReALM is used. This can be done by monitoring the pupil location carefully during alignment and/or laterally translating the imaging interface to confirm the preview OCT B-scans are centered within the pupil rather than vignetting.

Software motion correction has an advantage in that it corrects motion in three dimensions, improves signal, and does not require hardware modifications needed for eye tracking. However, two or more volumes must be acquired. This requirement can result in lesser imaging success rates because older patients might suffer from dry eye, fixation fatigue, or postural discomfort in longer imaging sessions. We have found that these effects can be mitigated to a certain extent by continuously acquiring horizontal-fast and vertical-fast rasters, then selecting the datasets with minimal eye motion and no blinking. It is important to note that eye tracking can also be used with UHR SD-OCT and ReALM. Eye tracking would compensate transverse eye motion and could work with acquisition of only a single volume,[41–43] but would not correct axial motion. For future implementations, real-time axial eye tracking using the OCT signal[44] could also be integrated into the ReALM protocol to reduce the artifacts associated with excessive patient axial eye motion.

In conclusion, we have developed an UHR SD-OCT instrument which operates at A-scan rates up to 250 kHz. The axial resolution was 2.4 µm (full-width at half-maximum OCT signal amplitude) in tissue using the unshaped spectrum and 2.7 µm with spectral shaping. A hardware–software technique, ReALM, was developed to mitigate the limited imaging range inherent in UHR SD-OCT.

UHR SD-OCT imaging performance was evaluated at 128 kHz versus 250 kHz A-scan rates. Patients with nonexudative AMD were imaged at 128 kHz A-scan rate because high signal-to-noise ratio is required in the presence of ocular opacity. HD raster scans covering 9 mm × 6 mm with 241 horizontal B-scans of 1800 A-scans, could resolve the fine structures of the photoreceptors, RPE, and BM across a wide FOV and detect subtle alterations associated with AMD. Software cube volumes covering 6 mm × 6 mm or 9 mm × 9 mm area with 500 × 500 A-scans provided accurate representations of en face and cross-sectional lesion morphology in AMD. These advances should simplify clinical imaging workflow, decrease imaging times, and improve yield of high quality images. Improved visualization of photoreceptors, RPE, and BM promises to facilitate diagnosis and monitoring of AMD and other retinal diseases.

Acknowledgments

Supported by the National Institutes of Health (5-R01-EY011289-33), Air Force Office of Scientific Research (FA9550-15-1-0473), Beckman-Argyros Award for Vision Research, and Retina Research Foundation.

Disclosure: **B. Lee**, None; **S. Chen**, None; **E.M. Moult**, None; **Y. Yu**, None; **A.Y. Alibhai**, None; **N. Mehta**, None; **C.R. Baumal**, None; **N.K. Waheed**, Macula Vision Research Foundation (F); Topcon Medical Systems, Inc (F); Nidek Medical Products Inc (F); Optovue Inc (C); and Carl Zeiss Meditec Inc (F); **J.G. Fujimoto**, Optovue Inc (P, I); Carl Zeiss Meditec Inc (P); Topcon Medical Systems Inc (R)

† BL and SC have contributed equally to the presented work and therefore share first authorship.

References

1. Huang D, Swanson EA, Lin CP, et al. Optical coherence tomography. *Science*. 1991;254:1178–1181.
2. Swanson EA, Izatt JA, Hee MR, et al. In vivo retinal imaging by optical coherence tomography. *Opt Lett*. 1993;18:1864–1866.
3. Hee MR, Izatt JA, Swanson EA, et al. Optical coherence tomography of the human retina. *Arch Ophthalmol*. 1995;113:325–332.

4. Drexler W, Morgner U, Kartner FX, et al. In vivo ultrahigh-resolution optical coherence tomography. *Opt Lett*. 1999;24:1221–1223.
5. Drexler W, Morgner U, Ghanta RK, Kartner FX, Schuman JS, Fujimoto JG. Ultrahigh-resolution ophthalmic optical coherence tomography. *Nat Med*. 2001;7:502–507.
6. Leitgeb R, Drexler W, Unterhuber A, et al. Ultrahigh resolution Fourier domain optical coherence tomography. *Opt Express*. 2004;12:2156–2165.
7. Wojtkowski M, Srinivasan V, Ko T, Fujimoto J, Kowalczyk A, Duker J. Ultrahigh-resolution, high-speed, Fourier domain optical coherence tomography and methods for dispersion compensation. *Opt Express*. 2004;12:2404–2422.
8. Drexler W, Sattmann H, Hermann B, et al. Enhanced visualization of macular pathology with the use of ultrahigh-resolution optical coherence tomography. *Arch Ophthalmol*. 2003;121:695–706.
9. Schmidt-Erfurth U, Leitgeb RA, Michels S, et al. Three-dimensional ultrahigh-resolution optical coherence tomography of macular diseases. *Invest Ophthalmol Vis Sci*. 2005;46:3393–3402.
10. Pieroni CG, Witkin AJ, Ko TH, et al. Ultrahigh resolution optical coherence tomography in non-exudative age related macular degeneration. *Br J Ophthalmol*. 2006;90:191–197.
11. Khanifar AA, Koreishi AF, Izatt JA, Toth CA. Drusen ultrastructure imaging with spectral domain optical coherence tomography in age-related macular degeneration. *Ophthalmology*. 2008;115:1883–1890.
12. Chen Y, Vuong LN, Liu J, et al. Three-dimensional ultrahigh resolution optical coherence tomography imaging of age-related macular degeneration. *Opt Express*. 2009;17:4046–4060.
13. Schuman SG, Koreishi AF, Farsiu S, Jung SH, Izatt JA, Toth CA. Photoreceptor layer thinning over drusen in eyes with age-related macular degeneration imaged in vivo with spectral-domain optical coherence tomography. *Ophthalmology*. 2009;116:488–496 e482.
14. Witkin AJ, Vuong LN, Srinivasan VJ, et al. High-speed ultrahigh resolution optical coherence tomography before and after ranibizumab for age-related macular degeneration. *Ophthalmology*. 2009;116:956–963.
15. Povazay B, Apolonski A, Unterhuber A, et al. Visible light optical coherence tomography. *Coherence Domain Optical Methods in Biomedical Science and Clinical Applications VI*. 2002;4619:90–94.
16. Yi J, Chen SY, Shu X, Fawzi AA, Zhang HF. Human retinal imaging using visible-light optical coherence tomography guided by scanning laser ophthalmoscopy. *Biomed Opt Express*. 2015;6:3701–3713.
17. Chong SP, Bernucci M, Radhakrishnan H, Srinivasan VJ. Structural and functional human retinal imaging with a fiber-based visible light OCT ophthalmoscope. *Biomed Opt Express*. 2017;8:323–337.
18. Potsaid B, Gorczynska I, Srinivasan VJ, et al. Ultrahigh speed spectral/Fourier domain OCT ophthalmic imaging at 70,000 to 312,500 axial scans per second. *Opt Express*. 2008;16:15149–15169.
19. An L, Li P, Shen TT, Wang R. High speed spectral domain optical coherence tomography for retinal imaging at 500,000 Alines per second. *Biomed Opt Express*. 2011;2:2770–2783.
20. Wang R, Yun JX, Yuan X, Goodwin R, Markwald RR, Gao BZ. Megahertz streak-mode Fourier domain optical coherence tomography. *J Biomed Opt*. 2011;16:066016.
21. BOETTNER EA, WOLTER JR. Transmission of the ocular media. *Invest Ophthalmol Vis Sci*. 1962;1:776–783.
22. American National Standards Institute. *American National Standard for Ophthalmics - Light Hazard Protection for Ophthalmic Instruments (ANSI Z80.36 - 2016)*. Orlando, FL: Laser Institute of America; 2016.
23. American National Standards Institute. *American National Standard for Safe Use of Lasers (ANSI Z136.1 – 2014)*. Orlando, FL: Laser Institute of America; 2014.
24. Wojtkowski M, Kowalczyk A, Leitgeb R, Fercher AF. Full range complex spectral optical coherence tomography technique in eye imaging. *Opt Lett*. 2002;27:1415–1417.
25. Leitgeb RA, Hitzenberger CK, Fercher AF, Bajraszewski T. Phase-shifting algorithm to achieve high-speed long-depth-range probing by frequency-domain optical coherence tomography. *Opt Lett*. 2003;28:2201–2203.
26. Hendargo HC, McNabb RP, Dhalla AH, Shepherd N, Izatt JA. Doppler velocity detection limitations in spectrometer-based versus swept-source optical coherence tomography. *Biomed Opt Express*. 2011;2:2175–2188.
27. Kraus MF, Potsaid B, Mayer MA, et al. Motion correction in optical coherence tomography volumes on a per A-scan basis using orthogonal scan patterns. *Biomed Opt Express*. 2012;3:1182–1199.
28. Kraus MF, Liu JJ, Schottenhamml J, et al. Quantitative 3D-OCT motion correction with tilt and illumination correction, robust similarity measure and

regularization. *Biomed Opt Express*. 2014;5:2591–2613.
29. Camino A, Zhang M, Gao SS, et al. Evaluation of artifact reduction in optical coherence tomography angiography with real-time tracking and motion correction technology. *Biomed Opt Express*. 2016;7:3905–3915.
30. Zawadzki RJ, Cense B, Zhang Y, Choi SS, Miller DT, Werner JS. Ultrahigh-resolution optical coherence tomography with monochromatic and chromatic aberration correction. *Opt Express*. 2008;16:8126–8143.
31. Zawadzki RJ, Jones SM, Pilli S, et al. Integrated adaptive optics optical coherence tomography and adaptive optics scanning laser ophthalmoscope system for simultaneous cellular resolution in vivo retinal imaging. *Biomed Opt Express*. 2011;2:1674–1686.
32. Kocaoglu OP, Lee S, Jonnal RS, et al. Imaging cone photoreceptors in three dimensions and in time using ultrahigh resolution optical coherence tomography with adaptive optics. *Biomed Opt Express*. 2011;2:748–763.
33. Kocaoglu OP, Turner TL, Liu ZL, Miller DT. Adaptive optics optical coherence tomography at 1 MHz. *Biomed Opt Express*. 2014;5:4186–4200.
34. Chan A, Duker JS, Ishikawa H, Ko TH, Schuman JS, Fujimoto JG. Quantification of photoreceptor layer thickness in normal eyes using optical coherence tomography. *Retina*. 2006;26:655–660.
35. Birch DG, Wen Y, Locke K, Hood DC. Rod sensitivity, cone sensitivity, and photoreceptor layer thickness in retinal degenerative diseases. *Invest Ophthalmol Vis Sci*. 2011;52:7141–7147.
36. Abramoff MD, Mullins RF, Lee K, et al. Human photoreceptor outer segments shorten during light adaptation. *Invest Ophthalmol Vis Sci*. 2013;54:3721–3728.
37. Lu CD, Lee B, Schottenhamml J, Maier A, Pugh EN, Jr., Fujimoto JG. Photoreceptor layer thickness changes during dark adaptation observed with ultrahigh-resolution optical coherence tomography. *Invest Ophthalmol Vis Sci*. 2017;58:4632–4643.
38. Yun SH, Tearney G, de Boer J, Bouma B. Motion artifacts in optical coherence tomography with frequency-domain ranging. *Opt Express*. 2004;12:2977–2998.
39. Gotzinger E, Pircher M, Leitgeb R, Hitzenberger C. High speed full range complex spectral domain optical coherence tomography. *Opt Express*. 2005;13:583–594.
40. Baumann B, Pircher M, Gotzinger E, Hitzenberger CK. Full range complex spectral domain optical coherence tomography without additional phase shifters. *Opt Express*. 2007;15:13375–13387.
41. Sheehy CK, Yang Q, Arathorn DW, Tiruveedhula P, de Boer JF, Roorda A. High-speed, image-based eye tracking with a scanning laser ophthalmoscope. *Biomed Opt Express*. 2012;3:2611–2622.
42. Vienola KV, Braaf B, Sheehy CK, et al. Real-time eye motion compensation for OCT imaging with tracking SLO. *Biomed Opt Express*. 2012;3:2950–2963.
43. Braaf B, Vienola KV, Sheehy CK, et al. Real-time eye motion correction in phase-resolved OCT angiography with tracking SLO. *Biomed Opt Express*. 2013;4:51–65.
44. Cua M, Lee S, Miao D, et al. Retinal optical coherence tomography at 1 mum with dynamic focus control and axial motion tracking. *J Biomed Opt*. 2016;21:26007.